Delft University of Technology

Flexural pulse wave velocity in blood vessels

Gregoire, Sibylle; Laloy-Borgna, Gabrielle; Aichele, Johannes; Lemoult, Fabrice; Catheline, Stefan

Flexural pulse wave velocity in blood vessels ⊘

Sibylle Gregoire ; Gabrielle Laloy-Borgna ; Johannes Aichele ; Fabrice Lemoult ; Stefan Catheline

Check for updates

View Online

Export Citation

CrossMark
click for updates

Flexural pulse wave velocity in blood vessels

Sibylle Gregoire,[1,a)] iD Gabrielle Laloy-Borgna,[2] iD Johannes Aichele,[3] iD Fabrice Lemoult,[4] iD and Stefan Catheline[1] iD

[1]*LabTAU, INSERM, Université Lyon 1, Lyon 69003, France*

[2]*ImPhys, Technische Universiteit Delft, Delft 2628 CJ, The Netherlands*

[3]*Institute of Geophysics, ETH Zurich, Zürich 8092, Switzerland*

[4]*Institut Langevin, CNRS, Université PSL, Paris 75005, France*

ABSTRACT:

Arteriosclerosis is a major risk factor for cardiovascular disease and results in arterial vessel stiffening. Velocity estimation of the pulse wave sent by the heart and propagating into the arteries is a widely accepted biomarker. This symmetrical pulse wave propagates at a speed which is related to the Young's modulus through the Moens Korteweg (MK) equation. Recently, an antisymmetric flexural wave has been observed *in vivo*. Unlike the symmetrical wave, it is highly dispersive. This property offers promising applications for monitoring arterial stiffness and early detection of atheromatous plaque. However, as far as it is known, no equivalent of the MK equation exists for flexural pulse waves. To bridge this gap, a beam based theory was developed, and approximate analytical solutions were reached. An experiment in soft polymer artery phantoms was built to observe the dispersion of flexural waves. A good agreement was found bet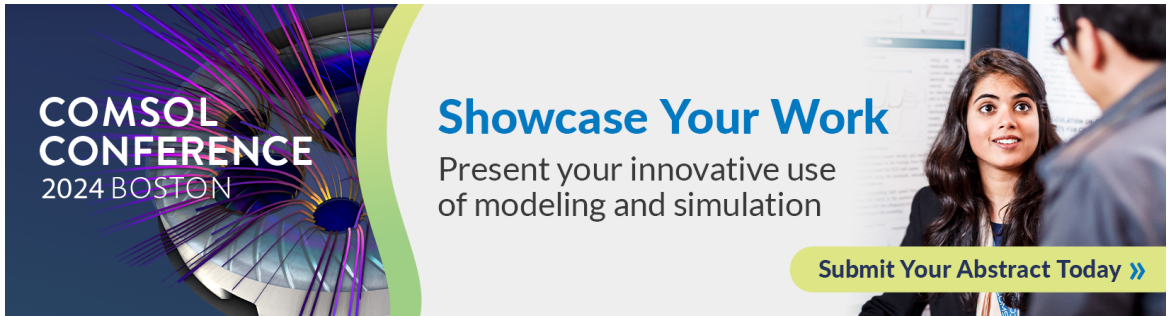ween the analytical expression derived from beam theory and experiments. Moreover, numerical simulations validated wave speed dependence on the elastic and geometric parameters at low frequencies. Clinical applications, such as arterial age estimation and arterial pressure measurement, are foreseen. © *2024 Acoustical Society of America*. https://doi.org/10.1121/10.0025855

I. INTRODUCTION

Cardiovascular disease is the world's leading cause of death, accounting for 32% of all deaths in 2019 (World Health Organisation, 2019). Risk factors, such as smoking, hypertension, diabetes, ageing, and even alcohol consumption, have an impact on arterial elastic properties (Cheng *et al.*, 2002; Hwang *et al.*, 2022). The stiffening of blood vessels, known as arteriosclerosis, has been proven to be a predictor of cardiovascular diseases (Cheng *et al.*, 2002; Laurent *et al.*, 2001; Sutton-Tyrrell *et al.*, 2005).

Assessing arterial stiffness provides valuable insights into the cardiac health of the patient. To evaluate and monitor arterial elasticity, current gold standard techniques are based on measuring the velocity of the arterial pulse wave (Willum-Hansen *et al.*, 2006).

This wave is emitted by the heartbeat and was first described by in Young (1809). Each heartbeat results in a pressure increase and a deformation of the aorta that propagates throughout the arterial tree. The propagation velocity of these guided waves is driven by the elasticity of the arterial walls. The stiffer an artery, the faster the pulse wave will travel.

There are primarily two methods for measuring pulse wave speed. The first method consists of measuring the time required for the pulse to travel from the carotid artery to a limb. The approximate distance covered is estimated using measurements on the surface of the body. This approach provides a fast, cost-effective, and global average of pulse wave speed (Hwang *et al.*, 2022; Laurent *et al.*, 2001).

The second method is employed for local measurements. It consists of tracking the pulse wavefront as it travels in the carotid artery using ultrafast ultrasound imaging (Couade *et al.*, 2011; Vappou *et al.*, 2010). In the case of shallow blood vessels, such as coronary arteries, rather than tracking the natural pulse wave, acoustic radiation force impulse (ARFI) can be used to generate guided waves within the vessel (Bernal *et al.*, 2011; Couade *et al.*, 2010). However, tracking ARFI and the natural pulse wave with ultrasound requires a high frame rate to follow a fast wave on a rather small field of view.

Once the pulse wave speed is estimated, the corresponding elasticity is computed using the Moens Korteweg (MK) equation. It was found in the 1870 s by Resal (1875), Isebree Moens (1878), and Korteweg (1878), and is the current gold standard. It was derived using general linear elasticity theory (Lamb, 1897) and fluid mechanics (Thorley, 1969; Tijsseling, 1995) and hypothesizes an infinite, homogeneous, thin tube filled with an inviscid fluid (Nichols and O'Rourke, 2012).

The heartbeat can be observed as an impulse propagating into the arterial tree with a broad spectrum. According to the general theory of elasticity, one can expect an infinity of modes propagating in the tube. In practice, the real

a)Email: sibylle.gregoire@inserm.fr

bandwidth of heartbeats only allows a few modes, of which only three remain at low frequency: an axisymmetric wave, which is also called breathing mode; an antisymmetric wave, which is also called flexural wave, and a torsional wave (Royer and Valier-Brasier, 2022). Up to now, research in angiography mainly focuses on the breathing mode, which is widely called the pulse wave. The two latter modes have so far been overlooked in clinical research, and the torsional mode still remains to be observed. *In vivo* observation of flexural waves was recently reported for the retinal arteries using optics and for the carotid artery using ultrasound imaging (Laloy-Borgna *et al.*, 2023).

Unlike the breathing mode, the flexural wave in a tube exhibits frequency dispersion. Its velocity plunges toward zero as the frequency decreases. At physiological frequencies, the flexural mode is much slower than the breathing mode. The slower the wave speed, the easier it is to measure. With slow imaging devices, such as X-ray, full field optical coherence tomography, or real-time magnetic resonance imaging (MRI), the wave speed measurement, thus, becomes possible. With fast imaging devices, like ultrafast ultrasound imaging, the velocity measurement becomes more precise at lower speeds. To sum up, the velocity of the flexural wave is an excellent candidate to assess and monitor arterial elastic properties.

However, although the breathing mode speed is related to the vessel Young modulus through the MK equation, to our knowledge, no such equation was formulated for the flexural wave. Therefore, it is the aim of this paper to find an equation relating flexural wave propagation and blood vessel elasticity. Such a relation paves the way to improved blood vessel elastography.

The usual approach to describe the propagation of guided waves is to use general linear elastic theory. In particular, for isotropic media, the case of waves travelling into a cylinder (Pao and Mindlin, 1960), a tube (hollow cylinder; Gazis, 1959), and a fluid filled tube (Berliner and Solecki, 1996) have been described. For these cases, linear elastic theory results in a system of equations describing the wave propagation, which can be numerically solved by optimisation methods (Gazis, 1959; Nishino *et al.*, 2001) or simulated through finite elements (FEs; Couade *et al.*, 2010; Marzani *et al.*, 2009; Shahmirzadi *et al.*, 2012). To our knowledge, no analytic formula exists to describe flexural guided waves propagation in fluid filled tube.

In this paper, an optical setup is developed to image flexural wave propagation in soft polymer artery phantoms. The low-frequency dispersion of the flexural mode of propagation is observed for a soft cylinder, hollow tube, and fluid filled tube. These idealized geometries allow linking pulse wave speeds in humans to the Young modulus, the physical parameter for arterial stiffness. We propose an analytical approach where arteries are modelled as beams through Euler Bernoulli theory. Indeed, it is established that the Euler Bernoulli theory, which was developed in the late 18th century, is the low-frequency limit of the general linear theory (Graff, 1975). Given the bandwidth of heartbeats,

flexural waves barely reach 20 Hz for *in vivo* observation (Laloy-Borgna *et al.*, 2023). It is, thus, a reasonable assumption to choose Euler Bernoulli theory to describe wave propagation in blood vessels.

II. OPTICAL ELASTOGRAPHY IN ARTERIAL BLOOD VESSEL PHANTOMS

To link flexural wave velocity to waveguide elasticity, an optical setup has been developed to observe flexural wave dispersion in soft cylinders, soft tubes, and water filled soft tubes.

A. Samples

Artery phantoms are produced using polyvinyl alcohol (PVA) in cylindrical or tubular molds (for more experimental details, please refer to Sec. VIII). Sample dimensions are measured using a caliper. Two samples are characterized: a cylinder of radius 8 mm and a tube of internal radius 6 mm and thickness 2 mm. All samples have a length of 20 cm. To probe the elasticity of the samples, a different, nonoptical, measurement method is used: ultrafast ultrasound imaging (see Sec. VIII for more experimental details). The tube and cylinder are found to have a shear wave velocity of $c_s \approx 4 \pm 1$ m/s.

B. Experimental setup

Figure 1(a) describes the experimental setup used to generate waves in the PVA tubes: a shaker, driven by an arbitrary waveform generator, is placed in contact with the phantom. The generator sends a sweep of frequency from 1 to 50 Hz. The phantom is positioned in front of a lighting table. The shaker is placed at the side of the tube to enhance its bending rather than its compression. The camera records at 100 fps. An example of a raw image obtained is displayed in Fig. 1(b).

Once the camera has recorded the image stack, the local displacement is computed. Figure 1(c) displays the displacement in each point for an arbitrary time step. Only displacements in the y direction are computed. Details of the post processing can be found in Sec. VIII. The edges of the phantom are moving as a block, which tends to indicate that the flexural mode is dominant over the breathing mode. Taking into account the symmetry of the modes, the displacements which correspond to flexion are isolated.

Unlike the symmetric pulse wave, the flexural pulse wave is dispersive. Its phase velocity depends on the frequency. To validate a theoretical or numerical model of its propagation, one needs a precise measurement of its dispersion.

C. Correlation spectroscopy for dispersion computation

To retrieve the dispersion curve of a specific mode, the usual approach found in the literature (Bernal *et al.*, 2011; Couade *et al.*, 2010; Maksuti *et al.*, 2016) is a two-dimensional (2D) fast Fourier transform of the raw image

J. Acoust. Soc. Am. **155** (5), May 2024
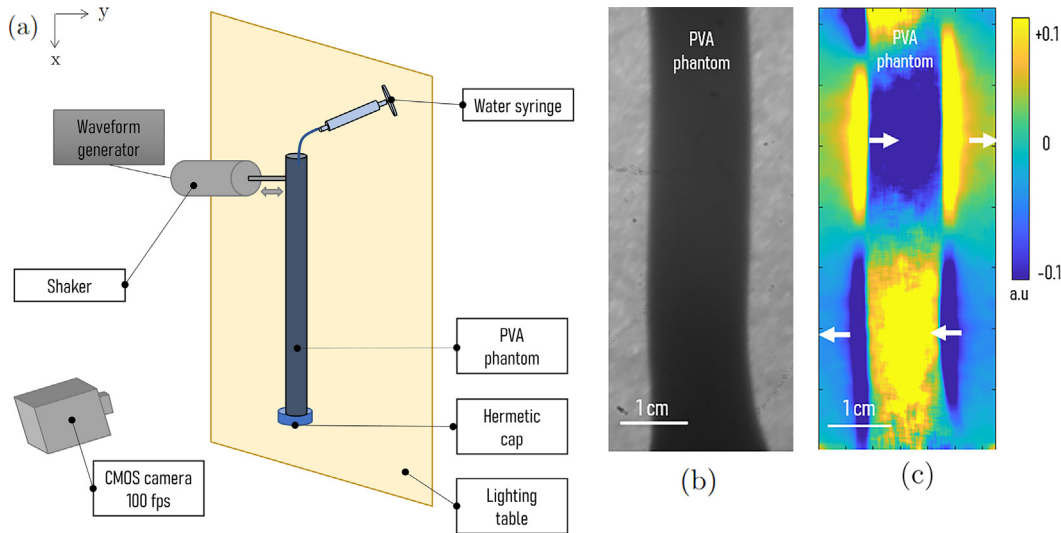
Gregoire *et al.* 2949

FIG. 1. (Color online) Experimental setup used to generate waves in the PVA tubes is shown in (a) a shaker, driven by an arbitrary waveform generator, is placed in contact with a phantom. This phantom is positioned in front of a light table. Displacement films are recorded using a complementary metal-oxide semiconductor (CMOS) camera. The shaker moves along the y axis while gravity is aligned with the x axis. (b) Raw optical image and (c) corresponding displacement field are displayed.

stack. The signal is plotted in the *f-k* space. There, branches corresponding to different modes can be discriminated. This method is not applicable in our experiments because of the limited size of the field of view. Direct measurement of the wave vector at each frequency is not possible. To measure the wave vector at each frequency, a correlation based approach is used. It was first developed in the scope of noise correlation elastography and then adapted for spectroscopy analysis (Ganeau *et al.*, 2023; Laloy-Borgna *et al.*, 2023).

Let us consider the displacement, $\phi(t)$, in two points, A and B, on the axis of the tube. Temporal correlation between ϕ_A and ϕ_B is noted as R_{AB}. Fourier transform of the displacements, $\underline{\phi_A(f)} = |\phi_A(f)|e^{iarg(\phi_A(f))}$, $\underline{\phi_B(f)} = |\phi_B(f)|e^{iarg(\phi_B(f))}$ are computed. The Fourier transform of the intercorrelation, $\underline{R_{AB}}$, is the cross-spectral density [Eq. (1)],

$$\underline{R_{AB}(f)} = \phi_A(f)\overline{\phi_B(f)}. \tag{1}$$

Using modulus and argument description of the displacement's Fourier transform and taking the real part of $\underline{R_{AB}}$, Eq. (2) is obtained. To whiten the spectrum, only the cosine part of Real($\underline{R_{AB}}$) is considered,

$$\text{Real}(\underline{R_{AB}(f)}) = |\phi_A(f)||\phi_B(f)| \cos(\arg\phi_A(f)$$
$$- \arg\phi_B(f)). \tag{2}$$

The above phase correlation is calculated at a given point A of the fiber and for all possible distances between point A and point B. The spatiotemporal correlation at one frequency is obtained. To spatially average the results, iteration along the axis of the tube is made, and a single averaged correlation is obtained for each frequency.

For an undamped single harmonic plane wave travelling in the media, one expects a sinusoidal shape (Wapenaar *et al.*, 2010). In our case, the propagation is that of damped

harmonic plane waves, where the spatial frequency of the sinusoidally shaped correlation is the wavelength of the plane wave. A sinusoidal fit is performed on the correlation at each frequency to obtain the wavelength (λ) at each frequency (f). Phase velocity, V_Φ, is then computed to be $V_\Phi = \lambda f$.

Figure 2(a) displays the spatiotemporal correlation map obtained experimentally for a hollow tube. Each line corresponds to a spatiotemporal correlation at one frequency. Figure 2(b) is a cut at $f = 10$ Hz of the above map. The spatiotemporal correlation for $f = 10$ Hz is plotted as a black plain line, and the sinusoidal fit is plotted as a dotted red line. The phase velocity is computed using the estimated wavelength of the sinusoidal fit. The corresponding dispersion curve is displayed in the bottom right of Fig. 2(a).

At this stage, we have an experimental setup enabling us to measure the dispersion of flexural waves in artery phantoms at the frequencies at which they were observed *in vivo*. Let us look now at the theory of its propagation.

III. THEORY OF FLEXURAL WAVES PROPAGATION, A BEAM APPROXIMATION

The Euler Bernoulli beam theory is a simplification of the linear general theory of elasticity. It specifically focuses on one-dimensional solids, known as beams, where two dimensions are much smaller compared to the third dimension. In this theory, the behavior of the beam is reduced to its neutral axis, which is also called the mean fiber. The primary assumption, known as the Navier-Bernoulli hypothesis, posits that a plane section normal to the mean fiber at rest remains plane and normal to the mean fiber during bending. Results obtained are recalled for a tube according to Graff (1975). In the present context of describing arterial bending, this theory will be employed to investigate the
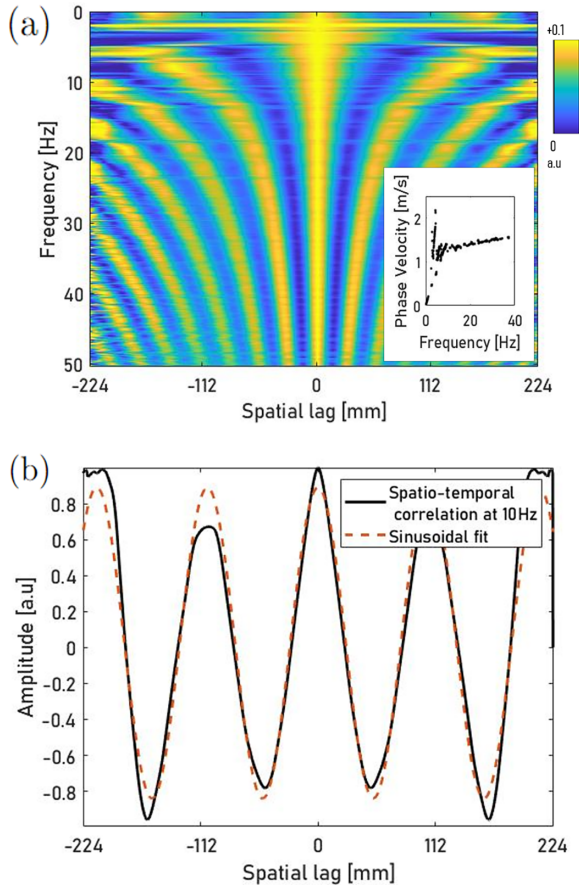
FIG. 2. (Color online) (a) Spatio-temporal correlation $R(f)$ for all frequencies is shown, where the bottom right inset is the obtained dispersion curve. (b) Spatio-temporal correlation at $f = 10$ Hz appears as plain black line and sinusoidal fit appears as dotted red line.

low-frequency behavior of a tube under either pure compression or pure bending.

A. Beam under pure compression

Let us consider an infinite, homogenous, and isotropic beam of arbitrary section, $S(x)$, as shown in Fig. 3(a). The beam is submitted to a purely longitudinal stress, σ, supposed to be homogeneous on its section. Volumetric, body forces are neglected.

On the one hand, considering a small segment, dx, of the beam, the second law of Newton, stated in Eq. (3), where u is the longitudinal displacement and ρ_s is the density of the beam gives

$$\rho_s \frac{\partial^2 u}{\partial t^2} = \frac{\partial \sigma}{\partial x}. \tag{3}$$

On the other hand, Hooke's law, stated in Eq. (4), where E is the Young's modulus of the beam, gives

$$\sigma = E \frac{\partial u}{\partial x}. \tag{4}$$

Merging Eqs. (3) and (4) together, one obtains the wave equation of the propagation of the compression stress in the beam, i.e., the breathing mode,

$$\frac{\partial^2 u}{\partial t^2} = \frac{E}{\rho_s} \frac{\partial^2 u}{\partial x^2}. \tag{5}$$

Considering the propagation of plane harmonic waves, the phase velocity, v_B, follows from Eq. (6). The phase
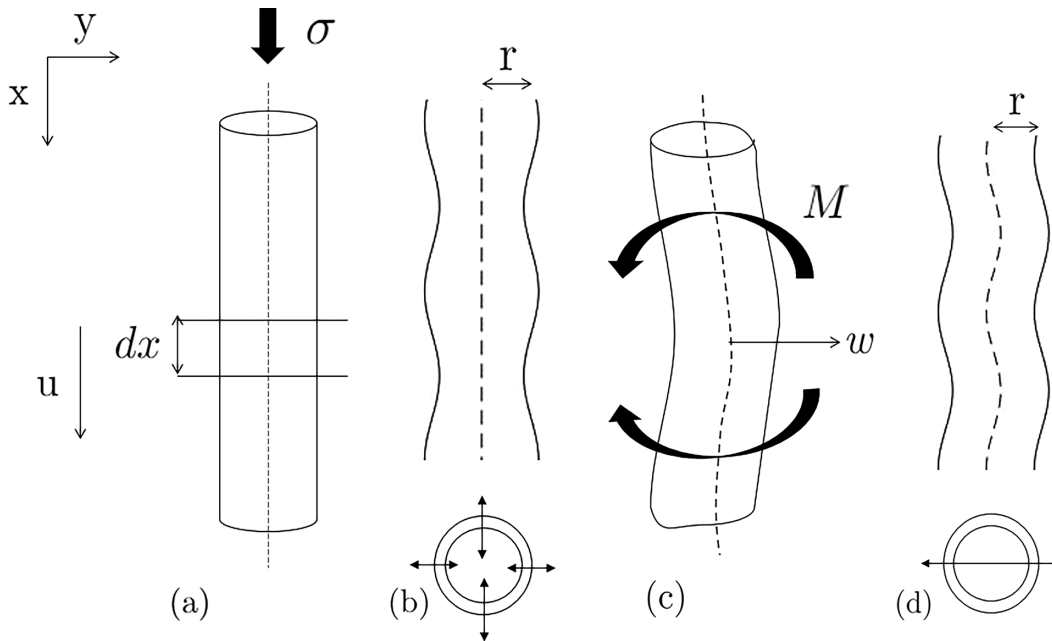
FIG. 3. Cylinder undergoing compression (a) and pure bending (c) is displayed. u, w are displacements in the x, y directions, respectively, the dotted line is the mean fiber of the beam, σ is the stress in the x direction, and M is the bending moment in the xy plane. Displacement polarisations are shown in the planes xy (up) and xz (down) for the breathing mode (b), which is axisymmetric with respect to the mean fiber in dotted line, and for the flexural mode (d), which is antisymmetric with respect to the mean fiber.

J. Acoust. Soc. Am. **155** (5), May 2024

Gregoire *et al.* 2951

velocity is nondispersive and, thus, no distortion of the wavefront happens. Furthermore, it is independent of shape parameters of the beam. This result is valid for all types of cross sections as long as the stress is uniformly distributed. In particular, it is valid for cylinders and tubes,

$$v_B = \sqrt{\frac{E}{\rho_s}}. \tag{6}$$

The polarisation of the breathing mode is displayed in Fig. 3(b), where the compression wave is axisymmetric with respect to the mean fiber.

B. Beam under pure bending

The beam is now submitted to a bending moment, M, as shown in Fig. 3(c). Computing the deformation of the mean fiber, Hooke's law is stated in Eq. (7). I is the second moment of area of the beam cross section, S, and w is the radial displacement,

$$M = -EI \frac{\partial^2 w}{\partial x^2}, \tag{7}$$

The second law of Newton on a small segment, dx, is stated as Eq. (8). Combining Eqs. (7) and (8), the wave equation (9), is obtained,

$$\rho_s S \frac{\partial^2 w}{\partial t^2} = \frac{\partial^2 M}{\partial x^2}, \tag{8}$$

$$\rho_s S \frac{\partial^2 w}{\partial t^2} = -EI \frac{\partial^4 w}{\partial x^4}. \tag{9}$$

Now, a harmonic plane wave, $w(x,t) = A \exp i(2\pi f t - kx)$, where k is the wave vector, f is the frequency, and t is the time considered. The wave vector is related to pulsation through the equation of dispersion (10), which is valid for any cross section with a homogeneous repartition of stress. In particular, it is valid for cylinders and tubes,

$$k^4 = 4\pi^2 f^2 \frac{\rho_s S}{EI}. \tag{10}$$

For a cylinder of radius r, $S = \pi r^2$, $I = \pi r^4/4$, using Eq. (10), the dispersion equation in terms of the phase velocity [Eq. (11)] is found,

$$v_F(\text{Cylinder}) = \sqrt{\pi f r \sqrt{\frac{E}{\rho_s}}}. \tag{11}$$

For a tube, where r_e is the exterior radius and r_i is the internal radius, $S = \pi(r_e^2 - r_i^2)$ and $I = \pi(r_e^4 - r_i^4)/4$. A thin tube is considered with $r_i, r_e \gg h$, where $h = r_e - r_i$ is the thickness. With r the mean radius of the tube, we have for a thin tube $r \approx r_e \approx r_i$. By performing a limited expansion to first order in h/r, we obtain the equation of dispersion,

$$v_F(\text{Tube}) = \sqrt{\sqrt{2}\pi f r \sqrt{\frac{E}{\rho_s}}}. \tag{12}$$

Unlike the breathing mode, the flexural mode in a tube is dispersive. The velocity increases with frequency as a square root. It depends on a geometric parameter of the tube, r, which is its mean radius.

The polarisation of the flexural mode is displayed in Fig. 3(d), where the flexural wave is antisymmetric with respect to the mean fiber.

It is worth noticing that the flexural wave in a thin tube is slightly faster by a factor $\sqrt{\sqrt{2}}$ than that in a cylinder of the same radius and elasticity.

C. On the valid frequency range of the Euler Bernoulli beam theory

The main assumption of the Euler Bernoulli beam theory is called Navier-Bernoulli: a plane section normal to the mean fiber at rest remains plane and normal to the mean fiber during deformation. The inertia of the deformation of the section due to shear forces and the rotational bending effect is neglected in Eqs. (3) and (8). As frequency increases, the wavelength becomes shorter, distances between opposing shear forces decrease, and the inertia of deformation of the section is not negligible anymore. In other words, as the wave propagates, it deforms the cross sections of the beam, slowing it down. As long as the wavelength is greater than the beam diameter, this slowdown is negligible. The frequency at which the inertia effect is not negligible anymore is the ring frequency, f_r, which is defined as the frequency above which the wavelength becomes shorter than the tube diameter. For a guided wave of any mode, propagating at a speed v, f_r is defined by Eq. (13),

$$f_r = \frac{v}{2r}. \tag{13}$$

D. Fluid filled tube: The added mass assumption

Let us now consider the case of a tube filled with a fluid of a density close to water density, ρ_w. Due to the presence of the liquid, the waves travelling down the tube have to transport additional mass with no elastic compensation. The inertia of the system is increased while elasticity remains identical. This is referred to as the added mass effect in fluid-structure interaction (Langre, 2001). We will assume that all other interactions can be discarded with regard to the added mass effect. In particular, the effect of the viscosity of the blood on the dispersion of the guided wave will be discarded.

For the flexural antisymmetric mode [see Fig. 3(b)], the walls of the tube move in block from one side to the other. There is no change in volume, and the effective cross section of the tube remains constant during the passage of the wave. All the fluid in the cross section contributes to the system's inertia. To quantify the added mass effect, let us

compute the mass increase between an empty tube and a fluid filled tube. A complete demonstration is given in the supplementary material.

The volumetric mass of an empty tube, ρ_e, is given by Eq. (14),

$$\rho_e = \rho_s \frac{(r_i + h)^2 - r_i^2}{(r_i + h)^2}.$$ (14)

However, blood vessels are soft tissues with densities close to those of the water, and we will approximate $\rho_s \approx \rho_w$. With this approximation, the volumetric mass of a fluid filled tube, ρ_f, is approximately that of the fluid such tht $\rho_f \approx \rho_w$. Equation (15) is the ratio of the volumetric mass of the fluid filled tube and the empty tube,

$$\frac{\rho_f}{\rho_e} = \frac{(r_i + h)^2}{(r_i + h)^2 - r_i^2}.$$ (15)

The typical radius to thickness ratio for blood vessels is around 0.2 (Müller *et al.*, 2008). This means that only thin tubes will be considered, where $r_i \gg h$. The mean radius of the tube, r, for a thin tube follows $r \approx r_i \approx r_e$. We, therefore, carry out a limited first-order development of Eq. (15) to obtain Eq. (16),

$$\frac{\rho_f}{\rho_e} \approx \frac{r}{2h}.$$ (16)

The apparent density observed by the wave in flexural mode is, hence, increased by an approximate factor, $r/2h$, when the tube is liquid filled.

Using the added mass approximation developed in Eq. (12) for an empty tube, we obtain the phase velocities of the flexural mode [Eq. (17)], which is valid for a fluid filled tube,

$$v_F(\text{Tube filled with fluid}) \approx \sqrt{2\pi f \sqrt{hr}\sqrt{\frac{E}{\rho}}}.$$ (17)

For the breathing mode, which is axisymmetric [see Fig. 3(d)], the volume of the tube changes as the wave passes through it, and the effective cross-sectional area of the tube increases as the wave expands the tube. The fluid set in motion by the passage of the tube is no longer only in the section. The apparent weight observed by the wave increased by a factor of $\alpha r/2h$, where $\alpha > 1$. With no added hypothesis on the pressure profile inside the fluid, the exact value of α cannot be determined,

$$v_B(\text{Tube filled with fluid}) \approx \sqrt{\frac{2h}{\alpha r}\sqrt{\frac{E}{\rho}}}.$$ (18)

It is worth noticing that Eq. (18) is the MK equation (Nichols and O'Rourke, 2012) with an added factor, $\sqrt{1/\alpha}$. To obtain α, MK equation is found by following the

demonstration by Resal (1875), and $\alpha = 4$ is found. A full demonstration is given in the supplementary material.

The comparison with the phase velocities found in the hollow tube [Eqs. (6) and (12)] highlights the effect of the fluid. For the breathing mode, fluid filling lowers the velocity by a geometric factor of $\sqrt{h/2r}$. For the flexural mode, fluid filling lowers the velocity by a geometric factor of $\sqrt{\sqrt{2h/r}}$. Adding fluid, thus, brings tube thickness into play. The dependency on the radius decreases from a square root.

To summarize, Eq. (17) is an equivalent of the MK equation for the flexural mode. This is the missing piece, the heart of the paper, which links the wave velocity and elastic modulus of the tube. We are now seeking to validate this expression by comparing the theory with optical experiments and numerical simulations.

IV. NUMERICAL SIMULATIONS

In addition to the experiments, FE simulations of flexural waves in cylinders, tubes, and fluid filled tubes are conducted using COMSOL Multiphysics (version 6.1). Simulations serve as an intermediary step between theory and experimentation and offer several advantages over pure theoretical or experimental results. First, they allow for the introduction of complexity: factors such as viscosity, anisotropy, fluid velocity, and changes in geometry or elasticity can be modelled. Second, simulations can facilitate parametric studies that may be challenging to implement in experiments. Additionally, the theory of beams is a simplification at low frequencies of the general theory of elasticity. Therefore, simulations help to explore the low-frequency limit beyond which the theory is no longer valid.

In our simulations, two sets of partial differential equations are solved through FE modelling: one set is for the elastic solid (the tube) and another set is for the fluid. The first set comprises the linear equations of the general theory of elasticity for solids as described in (COMSOL Multiphysics, 2023b), whereas the second set consists of the acoustic equations for a lossless fluid as described in COMSOL Multiphysics (2023a). The two modules are coupled by implementing the boundary conditions of a solid interacting with a fluid as described in COMSOL Multiphysics (2023c). Fluid was supposed to be still inside the tube. The complete framework employed in the simulations is described in Sec. VIII.

V. COMPARISON AND VALIDATION

A. Comparison with experiments and FE simulations

Figure 4 displays the evolution of the phase velocity with frequency for the flexural mode. The dots represent optical experimental data presented in Sec. II while the solid curves represent FE simulations. The dashed curves represent Euler Bernoulli based approximations, specifically Eq. (11) (for the cylinder), Eq. (12) (for the tube), and Eq. (17) (for the fluid filled tube). The results are plotted for the

J. Acoust. Soc. Am. **155** (5), May 2024
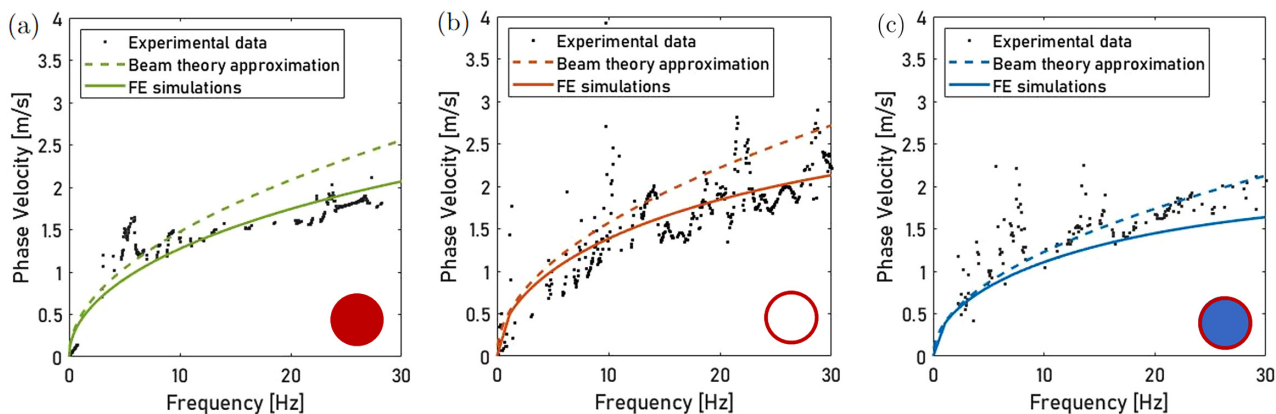
Gregoire *et al.* 2953

FIG. 4. (Color online) Dispersion curves of the flexural mode in a cylinder in PVA (a), a hollow tube of PVA (b), and in a water filled tube of PVA (c). Dots represent experimental data, plain curves are FEs simulated data and dotted curves are the analytic results from beam theory Eq. (11) for (a), Eq. (12) for (b), and Eq. (17) for (c).

cylinder in green [Fig. 4(a)], the tube in red [Fig. 4(b)], and the tube filled with fluid in blue [Fig. 4(c)].

At very low frequencies (<5 Hz), the wavelength becomes very long (around 10 cm) and approaches infinity when the frequency tends toward zero. At this point, due to the length of the tube and the field of view of the camera, accurate measurements are no longer possible, and the plotted data are not reliable.

Figure 4(a) is obtained in a cylinder. A good fit is achieved between the experimental data, FE simulations, and the approximation derived from beam theory. However, as the frequency increases, the limitations of the beam theory become evident, and it tends to overestimate the speed. This outcome is expected because the validity of the Navier-Bernoulli hypothesis decreases. As the frequency increases, it approaches the ring frequency, approximately 200 Hz for this geometry [Eq. (13)]. *In vivo*, the typical upper frequency of the bandwidth of a heartbeat is 10 Hz (Laloy-Borgna *et al.*, 2023). At 10 Hz, there is 13% of error between estimated and measured phase velocities.

The same results are obtained for the tube in Fig. 4(b). A good fit between experimental data, FE simulations, and the beam theory is observed at low frequencies. As the frequency increases, the theory of beams overestimates the speed. At 10 Hz, there is 17% of error between estimated and measured phase velocities.

As we fill the tube, i.e., as we move from Fig. 4(b) to Fig. 4(c), the dispersion curve shifts downward. The water is slowing down the wave. Once again, a good fit is retrieved between experimental data and FE simulations. Nevertheless, a greater discrepancy is observed compared to the previous case. This greater discrepancy could be a result of the tube not being completely filled. In fact, the closing valve was not completely airtight, and water could have been lost during the experiment. This would explain why the wave is slower in simulations than in the experiments.

A good fit between experimental data and beam theory derived approximation. The fit seems better than in the previous cases, but this result needs to be contrasted. Indeed, as the approximation tends to overestimate the speed, if the tube was not completely full, this would tend to improve the fit. At 10 Hz, there is 13% of error between estimated and measured phase velocities. *In vivo* estimation of the error using data from the carotid artery can be found in Sec. VI.

B. Parameter study using FE simulations

To assess the influence of multiple elastic parameters on flexural wave dispersion, FE simulations are employed. Figure 5 depicts the logarithm of the simulated flexural phase velocity of empty (red) and fluid filled (blue) tubes as functions of the logarithm of frequency [Fig. 5(a)], Young modulus [Fig. 5(b)], radius [Fig. 5(c)], and thickness [Fig. 5(d)] of the tube. In all simulations, the tubes have a bulk compression wave speed of $c_L = 1500$ m/s and a volumetric mass of $\rho = 1000$ kg/m^3.

Figure 5(a) focuses on the impact of the mean radius on phase velocity, where the frequency is fixed at a low value of 5 Hz. The mean radius ranges from 5 to 15 mm with a fixed thickness of $h = 2$ mm. The expected slope for an empty tube is 0.5; for a fluid filled tube, it is 0.25 [see Eqs. (12) and (17)]. The obtained slopes with simulations are 0.47 and 0.22, respectively.

In Fig. 5(b), the impact of the Young's modulus on the phase velocity is shown, where the frequency is fixed at a low value of 5 Hz. The mean radius is 7 mm, the thickness is $h = 2$ mm. Bulk shear wave speed ranges from 1 to 8 m/s. According to Eqs. (12) and (17), a regression coefficient of 0.25 is expected for empty and fluid filled tubes. With simulations in both cases, the coefficient obtained is 0.28.

In Fig. 5(c), the frequency spans from 0 to 50 Hz. The simulated tube has a bulk shear wave velocity of $c_s = 3$ m/s, a mean radius of $r_m = 7$ mm and a thickness of $h = 2$ mm. The dotted lines indicate the linear regressions corresponding to simulated data. According to the proposed analytic expressions [Eqs. (12) and (17)], the expected slopes for empty and fluid filled tubes are 0.5. The simulated slopes are 0.45 and 0.44, respectively.

Figure 5(d) focuses on the impact of the thickness on phase velocity. The frequency is fixed at 5 Hz and the

2954   J. Acoust. Soc. Am. **155** (5), May 2024
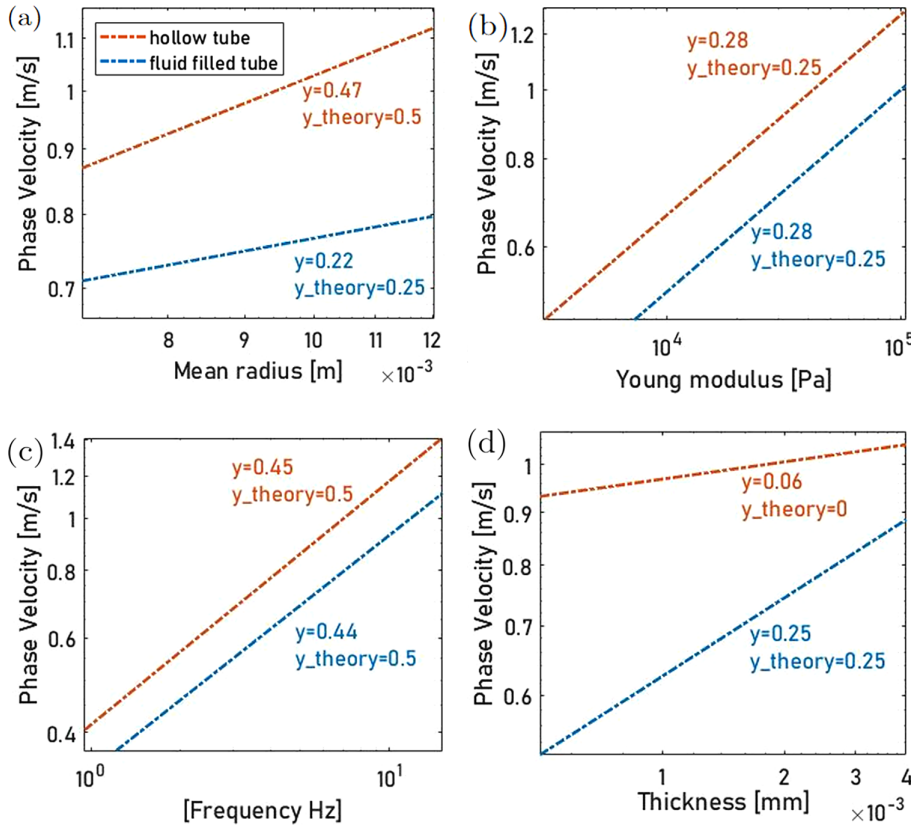
Gregoire *et al.*

FIG. 5. (Color online) Logarithmic plots display the dependence on the logarithm of the phase velocity and the logarithm of various parameters of interest: mean radius of the tube (a), Young's modulus (b), frequency (c), and tube thickness (d). Red curves are linear regression results for hollow tubes, and blue curves are linear regression results for fluid filled tubes. y is the regression coefficient found by simulations, y-theory is the regression coefficient expected by the analytical expression (12) for empty tubes and analytical expression (17) for fluid filled tubes.

external radius is fixed at $r = 8$ mm. The expected slope is 0 for an empty tube and 0.25 for a fluid filled tube [see Eqs. (12) and (17)]. The obtained slopes with simulations are 0.06 and 0.25, respectively.

VI. DISCUSSION

The experimental results show a good agreement between the approximated formulas derived from beam theory [Eqs. (11), (12), and (17)]. The excellent fit of the predicted parametric dependencies with the FE simulated data confirms that the flexural wave speed can be analytically described for low frequencies by Eq. (12) in a hollow tube and by Eq. (17) in a fluid filled tube.

Looking back to the medical application, flexural wave speed measurement can instantaneously be transformed to stiffness with Eq. (17). In Laloy-Borgna et al. (2023), flexural pulse waves were observed in the carotid artery and the retinal artery. Because of the lack of physical description of the flexural wave dispersion, the elasticity of the arteries could not be estimated. Equation (17) bridges this gap. Using the data of Laloy-Borgna et al. (2023), we can estimate the elastic modulus of the carotid artery using flexural waves, $E \approx 40$ kPa, and the retinal artery, $E \approx 0.5$ kPa.

In the carotid artery, the elastic modulus is quite low compared to typical values (Messas et al., 2013). The flexural wave velocity is obtained by considering a group velocity and evaluating the central frequency of the wave packet. For a more accurate value, it would be better to look at the phase velocity. Furthermore, the value obtained is an average of a single measurement on four different volunteers, most of whom are young. A specific study with a representative cohort should be performed to accurately estimate the elastic modulus of the carotid artery by flexural wave velocity. The aim here is to give an order of magnitude of the elastic modulus obtained via the flexural wave. In particular, the elastic modulus of the retinal arteries is estimated for the first time.

The assumption of linearity of stresses and strains is acceptable as the strains induced in the arteries by the flexural wave are of low amplitude: 0.5% of change of radius is observed in the carotid artery outside the systolic peak (Laloy-Borgna et al., 2023). It corresponds to 90% of a cardiac period. During 10% remaining, the transient systolic pressure creates an acoustoelastic effect. Quantitative measurements performed on signals acquired from the carotid artery of Laloy-Borgna et al. (2023) showed that the flexural velocity measurement was little affected by systolic nonlinearities.

This analytic relationship is only valid at low frequencies ($f \ll f_r$) when the Navier-Bernoulli approximation is verified. To have a more accurate formula for higher frequencies, lateral inertia and shear effects have to be taken into account for Eqs. (8) and (3). To quantify the error in vivo, we used, again, the data from Laloy-Borgna et al. (2023). At 7.5 Hz, a Young modulus of $E_B = 100$ kPa is found in the carotid artery through the breathing mode. Considering this value as a reference, the flexural velocity can be estimated [Eq. (17)]. There is an 18% error between this estimated value and the observed value in the carotid

J. Acoust. Soc. Am. **155** (5), May 2024

Gregoire et al.   2955

artery. To measure flexural waves for higher frequencies, the description by Euler Bernoulli could be replaced by that of Timoschenko (Haukaas, 2020). More accurate formulas could be derived for the breathing and flexural modes. However, as *in vivo*, the frequency content is dominated by heart rate harmonics, which are concentrated under 10 Hz, the Euler Bernoulli approach is sufficient.

Fluid-structure interactions have been simplified to the added mass effect. Initial blood velocity and viscosity have been neglected. A more complete analysis is possible by writing down the exact boundary conditions in the fluid, solid, and at the interface (Langre, 2001). However, as a first approach, the added mass effect seems predominant. Indeed, for the breathing mode, the MK equation is found again. FE simulations could be used to study the impact of viscosity and fluid flow. Providing enough computation speed, a numerical parameter optimisation could be implemented.

A blind spot in our study is the effect of the surrounding solid on flexural wave dispersion. We can assume that the surrounding solid induces an increase in the system's damping and inertia. This could lead to a slowing down of the flexural wave *in vivo* as well as a higher dissipation. FE simulations are foreseen to study this effect.

We assume the stress to be uniformly distributed over the cross section of the guide. In the case of sudden geometric rupture, such as a bifurcation, narrowing (stenotic site), or dilatation (aneurysmal site), impedance rupture should be considered. Local elasticity imaging using flexural waves is foreseen.

VII. CONCLUSION

After a heartbeat, all modes of propagation can exist within a blood vessel. Two modes were observed experimentally, the breathing mode and flexural mode. The breathing mode, which travels at the velocity of the MK, is well-known and used to probe the elasticity of arteries. This mode is not dispersive, and propagation is, thus, independent of frequency. Unlike the breathing mode, the flexural mode is dispersive. In this paper, the link between the phase velocity of the flexural wave and elasticity of the blood vessels was characterized; in other words, a flexural equivalent of the MK equation was derived. Our derivation relies on two main assumptions. The first assumption is shared with the MK approach and states that fluid only modifies inertia. The second assumption is that the Euler Bernoulli beam theory is verified. The validity of the analytic expression was verified experimentally and in FE simulations for physiological frequencies, far below the ring frequency of the vessel. The flexural mode has a major advantage over the breathing mode when it comes to probing vessel elasticity. Thanks to its dispersive behavior, it travels slower at low frequencies. In the 0 Hz limit, the phase velocity plunges to zero. With fast imaging devices, such as ultrafast ultrasound imaging, precision on the measured flexural pulse wave speed is, therefore, higher than that of the breathing mode. Local, precise, noninvasive measurement of blood vessel elasticity

could be reached. Flexural waves could image local narrowing of the blood vessels in real-time or local changes of impedance due to an atheromatous plaque. For slow imaging devices, elasticity measurements with the pulse wave are not feasible. The slowness of the flexural wave makes elasticity measurements with X rays, MRI, or full-field optical coherence tomography possible. Finally, an accurate, noninvasive estimation of arterial pressure is also envisioned.

VIII. MATERIAL AND METHODS

A. Experimental setup

A camera (Chronos 1.4, Kron Technologies, Burnaby, Canada), equipped with a zoom lens (Computar M6Z1212-3S, Computar, Mebane, NC), focuses on a PVA phantom. The phantom is secured by a clamp in front of a light table (Intimus 2001, Intimus, Markdorf, Germany). A shaker (The Modal Shop K2004E01, The Modal Shop, Cincinnati, OH), controlled by a waveform generator (RS Pro RSDG805, RS Pro, London, UK), makes contact with the phantom. Shaker output frequencies range from 0 to 50 Hz.

B. PVA phantoms

10% PVA (Sigma Aldrich, 363146-500G, Sigma Aldrich, St. Louis, MO) is heated until dissolution of PVA and mixed with 1% of graphite powder (Fisher Chemical 11385077, Thermo Fisher Chemical, Waltham, MA) under constant stirring. Then, the mixture is degassed under a vacuum chamber. It is poured into a home designed mold in polyvinyl chloride (PVC). The filled mold is then submitted to two freezing cycles (12 h at room temperature and 12 h in freezer). The phantom is removed from the mold and stored into water at room temperature.

C. Sample characterization using ultrafast ultrasound imaging

To assess the elasticity of the sample, a nonoptical measurement method is employed: ultrafast ultrasound imaging. This method used a high-frequency ultrasonic probe, specifically the L 22-14v (Verasonics Vantage, Kirkland, WA) with 128 elements, centered at 15 MHz. The probe is connected to a scanner (Verasonics Vantage) driven by MATLAB (The MathWorks, Natick, MA). The sample is imaged at a pulse repetition frequency (PRF) of 2000 Hz, and the acquisition time is 1 s. Simultaneously, a shaker (Cedrat APA600M, Cedrat Technologies, Meylan, France) vibrating at 800 Hz is brought into contact with the tube while imaging is conducted. A phase tracking algorithm is employed to recover the displacements in the tube. The Rayleigh velocity is measured using the time-of-flight method. Above the ring frequency [Eq. (13)], the breathing and flexural modes converged to the Rayleigh wave velocity. In this context, the Rayleigh wave velocity, denoted as c_R, is linked to the bulk shear wave speed, c_S, by the relation $c_R = \sqrt{5/6}c_S$ (Royer and Valier-Brasier, 2022).

D. Post processing

To compute the displacements field from the raw image stack, a phase tracking algorithm is used. It consists of computing the Hilbert matrix of the raw image stack to obtain the phase in each point. Then, the phase difference is computed frame by frame. It allows us to retrieve displacements of each point for each time step as displayed for an exemplary time in Fig. 1(c). The edges zone of the tube are cropped by hand and averaged to obtain the displacements of the left edge, ϕ_l, and right edge, ϕ_r, of the tube. The breathing mode is axisymmetric such that $\phi_l = -\phi_r$, whereas the flexural mode is antisymmetric such that $\phi_l = \phi_r$ [see Figs. 3(b) and 3(d) for polarisations, respectively]. To retain only the antisymmetric content, flexural displacements are defined as $\phi_f = \phi_r + \phi_l$.

E. FE simulations framework

COMSOL Multiphysics 6.1 is used with the following framework. The parameters of the simulations are the radius $r = 6$ mm; the thickness $h = 2$ mm; bulk compression wave speed, $c_L = 1500$ m/s; bulk shear wave speed, $c_S = 3$ m/s; and length of the tube, $a = 1$ mm. A component is created with two concentric cylinders as geometries, an acoustic domain in the center, and a solid mechanics domain in the shell. Both physics are linked by acoustic structure boundaries (COMSOL Multiphysics, 2023a). A Floquet periodic condition is added on the external sections of the cylinder. The Floquet periodicity unit cell is, therefore, a section of tube of length $a = 1$ mm. The k Floquet vector is incremented by a loop using MATLAB (The MathWorks, Natick, MA). A free triangular mesh is chosen. An eigenfrequency study is realised for each k vector. The solver is ARPACK (https://www.arpack.org/home), and search for eigenfrequency starts at 0 Hz.

SUPPLEMENTARY MATERIAL

See the supplementary material for the computation of mass increase between an empty tube and a fluid filled tube and the computation of the phase velocity of the breathing mode in a fluid filled tube following the work of Resal.

ACKNOWLEDGMENT

AUTHOR DECLARATION
Conflict of Interest

The authors have no conflicts to disclose.

DATA AVAILABILITY

The data that support the findings of this study are available from the corresponding author upon reasonable request.

Berliner, M. J., and Solecki, R. (**1996**). "Wave propagation in fluid-loaded, transversely isotropic cylinders. Part I. Analytical formulation," J. Acoust. Soc. Am. **99**(4), 1841–1847.

Bernal, M., Nenadic, I., Urban, M. W., and Greenleaf, J. F. (**2011**). "Material property estimation for tubes and arteries using ultrasound radiation force and analysis of propagating modes," J. Acoust. Soc. Am. **129**(3), 1344–1354.

Cheng, K. S., Baker, C. R., Hamilton, G., Hoeks, A. P. G., and Seifalian, A. M. (**2002**). "Arterial elastic properties and cardiovascular risk/event," Eur. J. Vasc. Endovasc. Surg. **24**(5), 383–397.

COMSOL Multiphysics (**2023a**). "Acoustic-structure boundary documentation," available at https://doc.comsol.com/5.5/doc/com.comsol.help.aco/aco_ug_multiphysics_couplings.13.03.html (Last viewed April 22, 2024).

COMSOL Multiphysics (**2023b**). "Linear elastic material documentation," available at https://doc.comsol.com/6.1/doc/com.comsol.help.sme/sme_ug_theory.06.026.html (Last viewed April 22, 2024).

COMSOL Multiphysics (**2023c**). "Pressure acoustics documentation," available at https://doc.comsol.com/5.5/doc/com.comsol.help.aco/aco_ug_pressure.05.004.html (Last viewed April 22, 2024).

Couade, M., Pernot, M., Messas, E., Emmerich, J., Hagège, A., Fink, M., and Tanter, M. (**2011**). "Ultrafast imaging of the arterial pulse wave," IRBM **32**(2), 106–108.

Couade, M., Pernot, M., Prada, C., Messas, E., Emmerich, J., Bruneval, P., Criton, A., Fink, M., and Tanter, M. (**2010**). "Quantitative assessment of arterial wall biomechanical properties using shear wave imaging," Ultrasound Med. Biol. **36**(10), 1662–1676.

de Langre, E. (**2001**). *Fluides et Solides* (*Fluids and Solids*) (Editions Ecole Polytechnique, Lausanne, Switzerland).

Ganeau, A., Legrand, F., Laloy-Borgna, G., Lafon, C., Lafond, M., and Catheline, S. (**2023**). "Shear wave elastography (SWE) for the measurement of lens elasticity in the context of monitoring a presbyopia treatment by ultrasonic cavitation," J. Acoust. Soc. Am. **153**(3_supplement), A68.

Gazis, D. C. (**1959**). "Three-dimensional investigation of the propagation of waves in hollow circular cylinders. II. Numerical results," J. Acoust. Soc. Am. **31**(5), 573–578.

Graff, K. F. (**1975**). *Wave Motion in Elastic Solids* (Oxford University Press, London, UK).

Haukaas, T. (**2020**). "Timoshenko beams," The University of British Columbia, Vancouver, Canada.

Hwang, C.-L., Muchira, J., Hibner, B. A., Phillips, S. A., and Piano, M. R. (**2022**). "Alcohol consumption: A new risk factor for arterial stiffness?," Cardiovasc. Toxicol. **22**(3), 236–245.

Isebree Moens, A. A. (**1878**). *Die Pulscurve* (*The Pulse Wave*) (Brill, Leiden), available at http://archive.org/details/diepulscurve00iseb (Last viewed April 22, 2024).

Korteweg, D. J. (**1878**). "Ueber die Fortpflanzungsgeschwindigkeit des Schalles in elastischen Röhren" ("On the velocity of propagation of sound in elastic tubes"), Ann. Phys. Chem. **241**(12), 525–542.

Laloy-Borgna, G., Puyo, L., Nishino, H., Atlan, M., and Catheline, S. (**2023**). "Observation of natural flexural pulse waves in retinal and carotid arteries for wall elasticity estimation," Sci. Adv. **9**(25), eadf1783.

Lamb, H. (**1897**). *Memoirs and Proceedings of the Manchester Literary & Philosophical Society, Velocity of Sound in a Tube* (The Society, Manchester), Vol. 42, pp. 1–502, available at https://www.biodiversitylibrary.org/item/111987 (Last viewed April 22, 2024).

Laurent, S., Boutouyrie, P., Asmar, R., Gautier, I., Laloux, B., Guize, L., Ducimetiere, P., and Benetos, A. (**2001**). "Aortic stiffness is an independent predictor of all-cause and cardiovascular mortality in hypertensive patients," Hypertension **37**(5), 1236–1241.

Maksuti, E., Widman, E., Larsson, D., Urban, M. W., Larsson, M., and Bjällmark, A. (**2016**). "Arterial stiffness estimation by shear wave elastography: Validation in phantoms with mechanical testing," Ultrasound Med. Biol. **42**(1), 308–321.

Marzani, A., Bocchini, P., Viola, E., Bartoli, I., Coccia, S., Salamone, S., Lanza, F., and Scalea, D. (**2009**). "A software for the computation of acoustic waves in cylindrical, plate and arbitrary cross-section waveguides," in *Congresso Nazionale sulle prove non distruttive Monitoraggio e diagnostica AIPnD*, Roma, Italy.

Messas, E., Pernot, M., and Couade, M. (**2013**). "Arterial wall elasticity: State of the art and future prospects," Diagn. Interventional Imag. **94**(5), 561–569.

Müller, B., Lang, S., Dominietto, M., Rudin, M., Schulz, G., Deyhle, H., Germann, M., Pfeiffer, F., David, C., and Weitkamp, T. (**2008**). "High-

J. Acoust. Soc. Am. **155** (5), May 2024

Gregoire *et al.* 2957

resolution tomographic imaging of microvessels," Proc. SPIE **7078**, 70780B.

Nichols, W. W., and O'Rourke, M. (**2012**). *McDonald's Blood Flow in Arteries: Theoretical, Experimental and Clinical Principles* (CRC Press, Boca Raton, FL).

Nishino, H., Takashina, S., Uchida, F., Takemoto, M., and Ono, K. (**2001**). "Modal analysis of hollow cylindrical guided waves and applications," Jpn. J. Appl. Phys. **40**(1R), 364.

Pao, Y.-H., and Mindlin, R. D. (**1960**). "Dispersion of flexural waves in an elastic, circular cylinder," J. Appl. Mech. **27**(3), 513–520.

Resal, H. (**1875**). "Note sur les petits mouvements d'un fluide incompressible dans un tuyau élastique" ("Note on small movements of an incompressible fluid in an elastic pipe") J. Math. Pures Appl. **2**, 342–344.

Royer, D., and Valier-Brasier, T. (**2022**). *Elastic Waves in Solids 1: Propagation*, 1st ed. (Wiley, New York).

Shahmirzadi, D., Li, R. X., and Konofagou, E. E. (**2012**). "Pulse-wave propagation in straight-geometry vessels for stiffness estimation: Theory, simulations, phantoms and *in vitro* findings," J. Biomech. Eng. **134**(11), 114502.

Sutton-Tyrrell, K., Najjar, S. S., Boudreau, R. M., Venkitachalam, L., Kupelian, V., Simonsick, E. M., Havlik, R., Lakatta, E. G., Spurgeon, H., Kritchevsky, S., Pahor, M., Bauer, D., and Newman, A. (**2005**). "Elevated aortic pulse wave velocity, a marker of arterial stiffness, predicts cardiovascular events in well-functioning older adults," Circulation **111**(25), 3384–3390.

Thorley, A. R. D. (**1969**). "Pressure transients in hydraulic pipelines," J. Basic Eng. **91**(3), 453–460.

Tijsseling, A. S. (**1995**). "Fluid-structure interaction in liquid-filled pipe systems: A review," J. Fluids Struct. **10**, 109–146.

Vappou, J., Luo, J., and Konofagou, E. E. (**2010**). "Pulse wave imaging for noninvasive and quantitative measurement of arterial stiffness *in vivo*," Am. J. Hypertens. **23**(4), 393–398.

Wapenaar, K., Draganov, D., Snieder, R., Campman, X., and Verdel, A. (**2010**). "Tutorial on seismic interferometry: Part 1—Basic principles and applications," Geophysics **75**(5), 75A195–75A209.

Willum-Hansen, T., Staessen, J. A., Torp-Pedersen, C., Rasmussen, S., Thijs, L., Ibsen, H., and Jeppesen, J. (**2006**). "Prognostic value of aortic pulse wave velocity as index of arterial stiffness in the general population," Circulation **113**(5), 664–670.

World Health Organisation (**2019**). "Cardiovascular diseases (CVDs)," available at https://www.who.int/fr/news-room/fact-sheets/detail/cardiovascular-diseases-(cvds) (Last viewed April 22, 2024).

Young, T. (**1809**). "I. The Croonian lecture. On the functions of the heart and arteries," Philos. Trans. R. Soc. London **99**, 1–31.

2958   J. Acoust. Soc. Am. **155** (5), May 2024

Gregoire *et al.*